ADVANCED FUNCTIONAL MATERIALS
www.afm-journal.de

Non Thermal-Driven Photocatalytic Ammonia Decomposition at Near-Room Temperature on a Plasmonic Nanocone Array

Thanh-Lam Bui, S. M. Hossein Hejazi, Jan Navrátil, Hana Kmentová, Petr Bábor, Olivier Henrotte, Luca Mascaretti, Matteo Bisetto, Stephen K. Sanders, Andrea Schirato, Michal Otyepka, Piotr Błoński, Tiziano Montini, Radek Zboril, Paolo Fornasiero, Alessandro Alabastri, Alberto Naldoni,* and Stepan Kment**

The efficient and sustainable production of hydrogen is crucial for the transition to a clean energy future. Ammonia (NH_3) is an attractive hydrogen carrier due to its high energy density and safe storage properties. However, conventional ammonia decomposition requires high temperatures, making the process energy-intensive and costly. Here, a plasmon-driven photocatalytic approach is presented for ammonia cracking at near-room temperature, utilizing a plasmonic antenna-reactor system made by a sharp tip anodic alumina oxide (AAO) array coated with a plasmonic Au film (antenna), decorated with Cu nanoparticles (reactors). This nanostructured catalyst harnesses surface plasmon resonances (SPRs) and generates hot carriers under visible light illumination, significantly enhancing the reaction efficiency. The best AAO@Au@Cu configuration exhibited a hydrogen evolution rate of 227 µmol h^{-1} $g_{Cu}{}^{-1}$ under 1 Sun irradiation at 35 °C. The enhanced activity is due to plasmonic non thermal effects, with the highest catalytic activity observed at 565 nm, corresponding to the SPR mode of the nanostructure. Mechanistic insights, supported by XPS, TOF-SIMS, and spin-polarized density functional theory calculations, suggested a multi-step NH_3 decomposition pathway involving NH_2NH_2 (hydrazine) and NH-NH intermediates. This study highlights the potential of plasmonic nanomaterials in revolutionizing low-temperature NH_3 decomposition, paving the way for sustainable hydrogen production at solar intensities.

1. Introduction

In the pursuit of sustainable energy development, minimizing carbon dioxide (CO_2) emissions from fossil fuel consumption has emerged as a global priority.[1–2] Hydrogen, often hailed as the "fuel of the future," stands out for its high energy density compared to alternative renewable energy sources such as methanol and ethanol.[3] Additionally, it offers significant environmental advantages, particularly when its production results in zero CO_2 emissions.[4–6] However, the high delivery costs, risk of leakage, and explosion hazards have posed significant challenges to the practical implementation of hydrogen energy technologies.[7–8]Ammonia is widely regarded as one of the most promising hydrogen carriers due to its low cost, high safety (with explosive concentration range of ammonia in air, i.e., explosion limits, of 15.7–27.4 v/v.%), and exceptional volumetric energy density (108 kg H_2 per m^3 NH_3 at 8.6 bar and 20°C),[9–10] efficient

T.-L. Bui, S. M. H. Hejazi, J. Navrátil, H. Kmentová, O. Henrotte, L. Mascaretti, M. Otyepka, P. Błoński, R. Zboril, S. Kment
Regional Centre of Advanced Technologies and Materials
Czech Advanced Technology and Research Institute (CATRIN)
Palacký University Olomouc
Šlechtitelů 27, Olomouc 779 00, Czech Republic
E-mail: stepan.kment@upol.cz

The ORCID identification number(s) for the author(s) of this article can be found under https://doi.org/10.1002/adfm.202505216

DOI: 10.1002/adfm.202505216

T.-L. Bui, S. M. H. Hejazi, R. Zboril, S. Kment
Nanotechnology Centre
Centre for Energy and Environmental Technologies
VSB-Technical University of Ostrava
17. listopadu 2172/15, Ostrava-Poruba 708 00, Czech Republic

P. Bábor
Central European Institute of Technology
Brno University of Technology
Purkyňova 656/123, Brno 612 00, Czech Republic

P. Bábor
Institute of Physical Engineering
Faculty of Mechanical Engineering
Brno University of Technology
Brno University of Technology
Technická 2, Brno 612 00, Czech Republic

transportation, storage, and easy separation from hydrogen gas flow.[11–13] Ammonia decomposition (Equation 1) is an endothermic reaction, and therefore it is favored at increasing temperatures. Moreover, ammonia conversion decreases at increasing pressure.

$$2NH_3 + \text{heat} \rightleftarrows 3H_2 + N_2 \quad (1)$$

The primary challenge associated to ammonia cracking for sustainable hydrogen production is thus the requirement for very high temperatures to achieve a complete reaction (equilibrium calculations show that a temperature of 400 °C is required to convert 99.1% of ammonia to its decomposition products at 0.1 MPa), making the process energy-intensive and costly.[14–16] Therefore, the development of novel efficient catalysts to operate ammonia decomposition at lower temperatures is essential for reducing energy consumption while enhancing safety and cost-effectiveness for practical ammonia decomposition.

Surface plasmon resonances (SPRs) in metallic nanomaterials have emerged as an exceptionally efficient mechanism to drive photocatalytic events, leveraging the generation of high-energy 'hot' carriers under visible light excitation.[17–18] Through the plasmon decay process, when nearby molecules are adsorbed onto the metal surface, hot carriers and near fields can transfer energy into the molecular electronic states, initiating various photocatalytic reactions, such as cross-coupling reactions or bond cleavage, at significantly lower temperatures than conventional thermal catalysis.[19–21] Non-linear optical effects in plasmonic nanomaterials, including amplification of near fields, make it possible to trigger the activation of molecular bonds under non-equilibrium conditions, opening new pathways for photocatalytic reactions.

Halas and colleagues have revolutionized ammonia decomposition by combining plasmonic and catalytic functionalities into antenna-reactor nanoparticles (e.g., Cu-Ru, Cu-Fe).[22–23] In the case of Cu-Ru antenna-reactor nanostructures, a temperature of 475 °C under high-intensity light irradiation (9.6 W cm^{-2}, ≈96 suns) has enabled quantitative ammonia decomposition. This was possible thanks to both the photoinduced thermal gradients and the hot electrons generated by the plasmonic Cu units, which resulted in a decrease of the activation energy compared to the value in thermal dark conditions. However, the precise attribution of the roles played by non-thermal and thermal effects in driving gas-phase photocatalytic reactions at high solar concentrations is challenging.[24–25] Additionally, the stability of plasmonic catalytic materials requires to be carefully considered for practical applications, as the sintering and aggregation of plasmonic nanoparticles at high temperatures can severely degrade catalytic performance and compromise long-term viability.[26]

Since the groundbreaking discovery of anodic aluminum oxide (AAO) by Masuda and Fukuda through a two-step anodization process, researchers worldwide have dedicated significant efforts to exploiting the unique properties of AAO templates for the fabrication of various nanostructures.[27] Unlike the intricate, time-consuming, and costly conventional lithography techniques, the high structural homogeneity of AAO—characterized by uniform nanopore diameter, length, and wall thickness—enables the fabrication of plasmonic nanoparticle arrays composed of Au, Ag, and Cu over large surface areas with high consistency and scalability.[28] Although the plasmonic materials deposited on the AAO platform have been applied for energy applications,[29–34] they have not been reported yet for the gas phase photocatalytic ammonia decomposition.[35]

In this study, plasmon-driven photocatalytic ammonia decomposition under 1 Sun illumination (100 mW/cm^2) was investigated using an antenna-reactor metasurface made by an array of plasmonic (Au-based) nanocones (NCs) supported on an AAO nanopatterned substrate and decorated with catalytic Cu nanoparticles. The optical properties of the whole system were investigated by electromagnetic simulations, revealing plasmonic resonances and peculiar near-field patterns throughout the NCs, strongly depending on the thickness of the Au layer. Efficient light absorption and localization of fields within the Cu nanoparticles enable to activate ammonia decomposition at near-room

L. Mascaretti
Department of Laser Physics and Photonics
Faculty of Nuclear Sciences and Physical Engineering
Czech Technical University in Prague
Břehová 7, Prague 11519, Czech Republic

M. Bisetto, T. Montini, P. Fornasiero
Department of Chemical and Pharmaceutical Sciences, Center for Energy Environment and Transport Giacomo Ciamiciam, INSTM Trieste Research Unit and ICCOM-CNR Trieste Research Unit
University of Trieste
Via L. Giorgieri 1, Trieste 34127, Italy

J. Navrátil
Department of Physical Chemistry
Faculty of Science
Palacký University Olomouc
17 listopadu 12, Olomouc 779 00, Czech Republic

S. K. Sanders, A. Alabastri
Department of Electrical and Computer Engineering
Rice University
6100 Main Street, Houston, TX 77005, United States
E-mail: alessandro.alabastri@rice.edu

S. K. Sanders
U.S. Army DEVCOM Army Research Laboratory-South
Oak Ridge Associated Universities
Houston, TX 77005, USA

A. Schirato
Dipartimento di Fisica
Politecnico di Milano
P.zza Leonardo da Vinci, 32, Milano 20133, Italy

A. Schirato
Department of Physics and Astronomy
Rice University
6100 Main Street, Houston, TX 77005, United States

M. Otyepka, P. Błoński
IT4Innovations
VŠB–Technical University of Ostrava
17. listopadu 2172/15, Ostrava-Poruba 708 00, Czech Republic

A. Alabastri
Laboratory for Nanophotonics Rice University
6100 Main Street, Houston, TX 77005, United States

A. Alabastri
Smalley-Curl Institute & Rice Advanced Materials Institute
Rice University
6100 Main Street, Houston, TX 77005, United States

A. Naldoni
Department of Chemistry and NIS Centre
University of Turin
Turin 10125, Italy
E-mail: alberto.naldoni@unito.it

temperature, and produce appreciable hydrogen evolution rates with good stability. The photocatalytic activity of the plasmonic NCs was systematically investigated by varying the excitation wavelengths and structural parameters of the plasmonic NCs, as well as the amount of Cu catalyst deposited. In contrast to previously reported bimetallic systems such as Cu–Fe and Cu–Ru,[23] which encounter a high energy barrier for N—N coupling (2.67–2.84 eV), our DFT calculations revealed that N—N bond formation occurs through the coupling of NH_x intermediates (e.g., NH and NH_2), bypassing the need for isolated N species. This pathway, with a maximum activation barrier of 1.13 eV, is compatible with solar-driven catalysis at ambient conditions and underscores the distinct mechanistic advantage of the Cu–Au interface under higher ammonia partial pressures. With high reproducibility and facile fabrication, this work provides a reliable strategy for leveraging plasmonic nanomaterials to efficiently convert light energy and drive catalytic reactions under out-of-equilibrium conditions.

2. Results and Discussions

2.1. Non-Lithographic Fabrication of Large-Scale Plasmonic Nanocone (NCs) Arrays

The fabrication of the plasmonic NCs array followed the process outlined in **Figure 1A**. Briefly, AAO template with terminating sharp tips was first prepared through a sequential electrochemical anodization of an alumina foil, followed by pore-widening steps. A detailed description of the entire process is provided in the Supporting Information and in Figure S1a (Supporting Information). Subsequently, two sputtering steps were performed to first overcoat the bare sharp tip AAO with a plasmonic Au film, and then deposit catalytic Cu nanoparticles, respectively. The plasmonic NCs were thoroughly characterized using field emission scanning electron microscopy (FE-SEM) and high-angle annular dark-field (HAADF) imaging to assess their morphology and elemental distribution. As shown in Figure S1 (Supporting Information), sharp and highly ordered tips were homogeneously formed on the surface of the AAO substrate, resulting in a well-defined hexagonal close-packed array. From top-view SEM images, the diameter and nanogap distance of adjacent tips were estimated as ≈16 and ≈41 nm, respectively, while the nanopore diameter and the internal wall thickness as ≈101 and ≈11 nm, respectively. Different plasmonic NC structures were fabricated by varying the Au sputtering time (40 s, 80 s, 120 s, and 160 s) while keeping the Cu sputtering time constant at 16 s. This approach aimed to deposit Cu in the form of nanoparticles acting as catalytic centers, and to control the thickness of the Au layer, thereby transforming the AAO template into a plasmonic antenna-reactor metasurface. Hereafter, these samples are referred to as AAO@40Au@16Cu, AAO@80Au@16Cu, AAO@120Au@16Cu, and AAO@160Au@16Cu, respectively. Figure 1B illustrates the morphology of our plasmonic NCs substrates, depicted in both top-view and tilted-view SEM images, following the metal deposition process. For better clarity, all parameter variations resulting from the Au sputtering process are visualized in Figure S2 (Supporting Information) and summarized in Table S1 (Supporting Information). Top-view SEM images reveal a progressive increase in the plasmonic NCs diameter from 22 to 26, 32, and 37 nm for the AAO@40Au@16Cu, AAO@80Au@16Cu, AAO@120Au@16Cu, and AAO@160Au@16Cu, respectively. Concurrently, the spacing between adjacent NCs decreased from 39 to 32, 27, and 20 nm, respectively. With increasing sputtering time, the orifice diameter of the AAO template also gradually narrowed to 93, 87, 81, and 75 nm. Additionally, the internal wall width between adjacent NCs expanded from 16 to 20, 25, and 29 nm, indicating the continuous deposition of metal onto the template. Large-scale SEM images (Figures S3–S6, Supporting Information) demonstrate the long-range periodicity of the NCs array over areas up to the centimeter scale, highlighting its tunability and the cost-effectiveness of this facile method for scalable fabrication. By adjusting the Au sputtering time, we can precisely control the dimensional parameters of plasmonic NCs, which is crucial for achieving the desired optical properties. To further investigate the influence of morphology on optical properties, as discussed in detail in the following chapter, the same metal sputtering conditions used for the sharp-tip AAO template were applied to a flat Al/Al_2O_3 substrate (Figure S7, Supporting Information). The SEM images revealed that irregularly-shaped plasmonic nanoparticles formed on the flat substrate, which is typical for a sputtering process on a rough surface, in contrast to the highly uniform plasmonic NCs array observed on the sharp-tip AAO template. This comparison underscores the critical role of morphological control in achieving structural uniformity, which significantly impacts optical performance, making the sharp-tip AAO template a superior platform for plasmonic photocatalysis. Furthermore, the influence of Cu sputtering time (ranging from 8 to 16 and 24 s) on the structural characteristics of distinct 80 s Au sputtering was systematically examined (shown in Figure S8, Supporting Information). In the following, special attention is given to the thorough characterization and analysis of the AAO@80Au@16Cu NC sample, as it exhibited the highest photocatalytic performance for ammonia cracking. The tilted-view SEM images in Figure 1B confirm the formation of vertically-aligned plasmonic NCs, demonstrating that the sharp-tip structure remained well-preserved throughout the sputtering process. The Au deposition follows an island growth and directional mode, as can be observed in Figure 1C and Figure S9 (Supporting Information). Consequently, the Au coverage decreases from the tip to the internal walls of the pores within the AAO structure. However, by increasing the sputtering time, a uniform coating of the tips was achieved, eventually leading to their complete coverage. Inductively coupled plasma mass spectrometry (ICP-MS) was employed to estimate the mass of Au and Cu for each sputtering condition separately. The measurements confirmed a linear increase in deposited mass with sputtering time, as expected (Figure S10, Supporting Information). The HAADF measurements with EDS elemental mapping of AAO@80Au@16Cu NCs were employed to visualize the internal structure, elemental distribution, and thickness on the sharp tip. Figure 1C presents a single AAO@80Au@16Cu NC, along with its EDS mapping. The metallic Au deposition fully covers the tip, while small Cu nanoparticles (≈3 nm in diameter) are dispersed on the Au layer surface. Figure S9 (Supporting Information) showcases an ensemble of plasmonic NCs to further illustrate their morphological properties. The nanopore exhibits a distinct conical shape, with its diameter gradually decreasing from

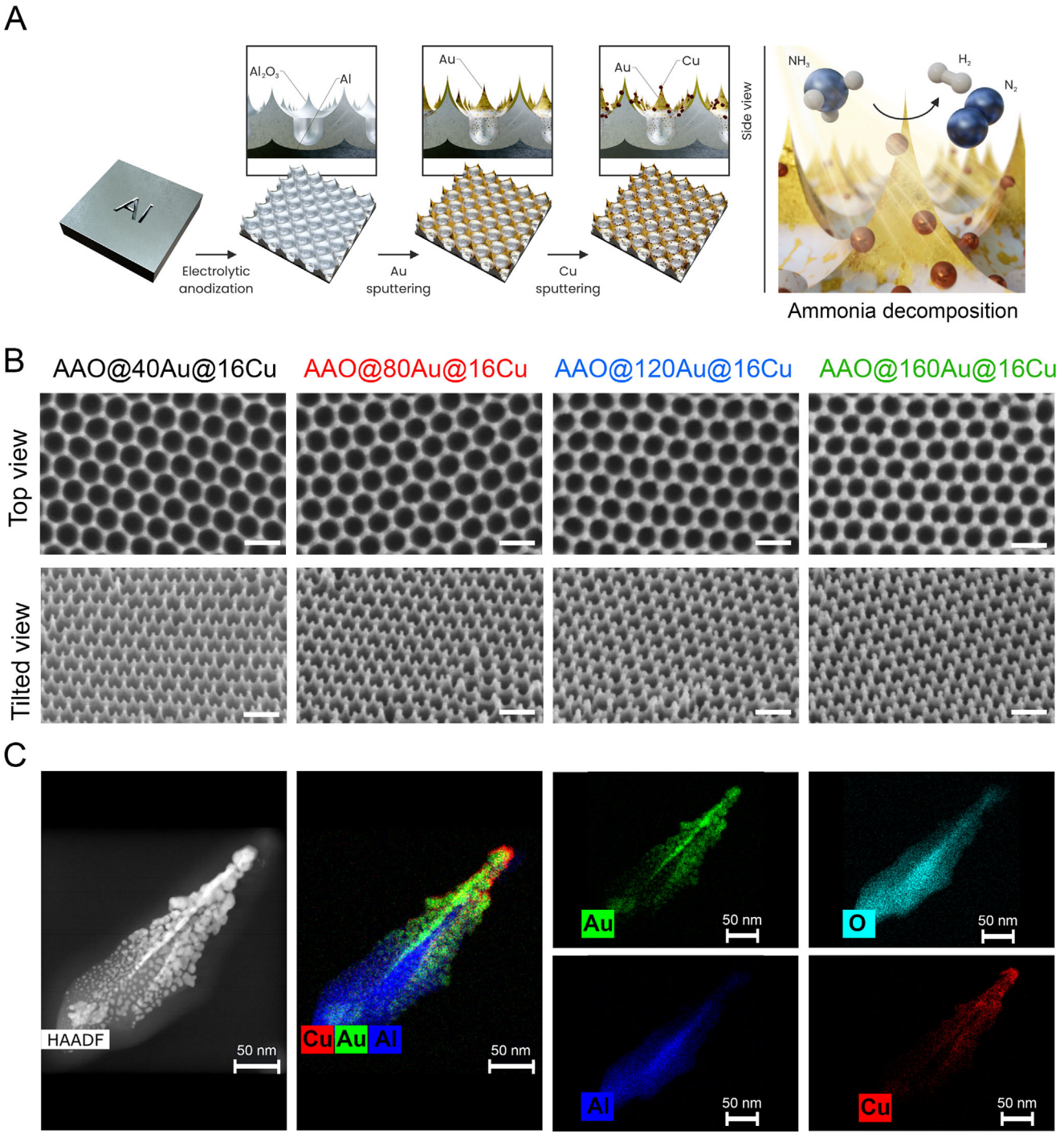

Figure 1. A) Schematics of the sequential fabrication steps for the plasmonic NCs array used in ammonia decomposition. B) SEM images at the top view and tilted view for AAO@40Au@16Cu, AAO@80Au@16Cu, AAO@120Au@16Cu, AAO@160Au@16Cu, together with increasing Au sputtering time from 40, 80, 120, 160, and fixed duration of 16s for Cu sputtering, all scale bars were 200 nm. C) The HAADF images of a representative single AAO@80Au@16Cu NC tip, along with elemental mapping showing the overlapped distribution of Au-Al-Cu and individual elements of O, Au, Al, and Cu.

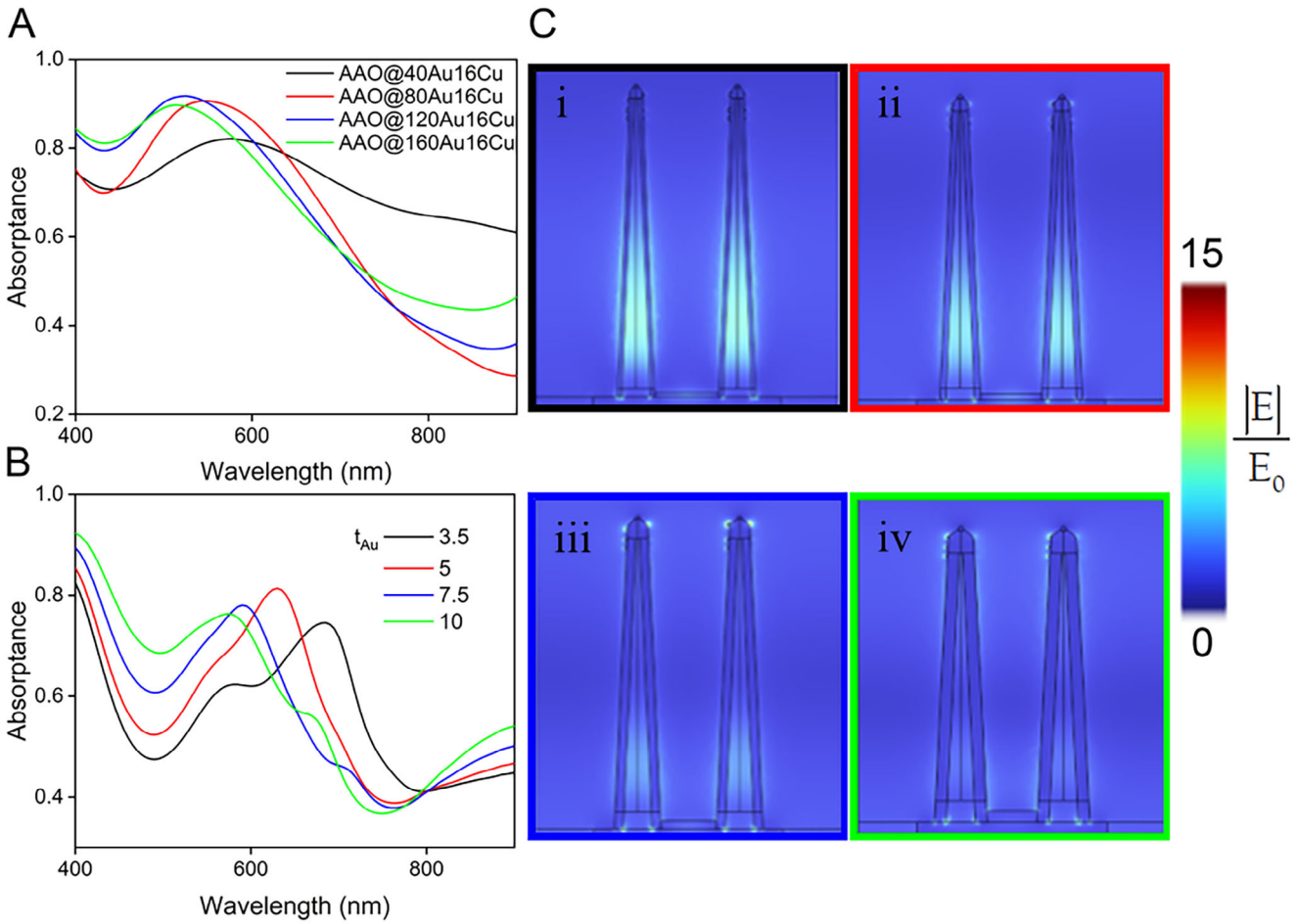

Figure 2. A) Experimental optical absorption spectra of plasmonic NCs with increasing Au sputtering time of 40, 80, 120, and 160 with fixed 16 s Cu sputtering time. B) Simulated absorption spectra of plasmonic NCs array with various thicknesses t_{Au} (as indicated by the legend, in nm) and accompanied by Cu nanoparticles near the tip. C) Spatial distribution of the near field enhancement of plasmonic NCs with different Au thickness (i-3.5, ii-5, iii-7.5, and iv-10 nm), evaluated at the corresponding absorbance peak.

the top to the bottom of the oxide layer, while the internal wall thickness correspondingly increases in the opposite direction.

2.2. Optical Properties of Plasmonic NCs Arrays

Figure 2 illustrates the optical properties of the plasmonic NCs. Notably, the bare sharp-tip AAO scaffold shows no absorbance in the visible region, indicating that the appearance of the SPR results from the following metal deposition (Figure S11, Supporting Information). To further explore the tunability of the system's plasmonic properties, the optical response was studied as a function of the Au deposition on the bare sharp-tip AAO, while the Cu deposition time was kept constant for 16 s. As shown in Figure 2A, the experimental absorptance peak undergoes a blue shift, progressively shifting from 585 nm to 552, 535, and 521 nm as the Au sputtering time increases from 40 to 80, 120, and 160 s, respectively. At 40 s sputtering time, the experimental absorptance of AAO@40Au@16Cu exhibits a broad and weak absorption, likely due to insufficient Au coverage on the nanostructured template. Notably, 80 s Au sputtering appears to be the optimal condition, yielding the strongest absorption intensity. However, as the Au sputtering time increases to 160 s, the spectra not only shift further to the blue region but also exhibit a significant decrease in absorbance intensity. This phenomenon can be attributed to the complex interplay between the Au thickness and the plasmonic resonance of the nanostructure, as ascertained by our electromagnetic simulations. In Figure 2B the simulated absorptance is shown (see Supporting Information and Figure S12 for details on the simulations), qualitatively resembling the same blue shift and non-monotonic trend as the measured absorptance. To explain this trend, in Figure 2C, we analyzed the near-field enhancement at the wavelength of peak absorption. As the thickness of the Au layer increases, there is less field build-up inside the AAO cones, leading to a decreasing absorptance. On the other hand, when the Au layer becomes too thin, despite the larger field build-up, the metallic layer is not thick enough to absorb a significant portion of light. Competition between these two effects leads to the maximum absorbance for a 5-nm thick layer. It is important to note that while Figure 2B,C illustrate the theoretical dependence of absorbance on gold thickness, the exact correlation between sputtered gold thickness and sputtering time

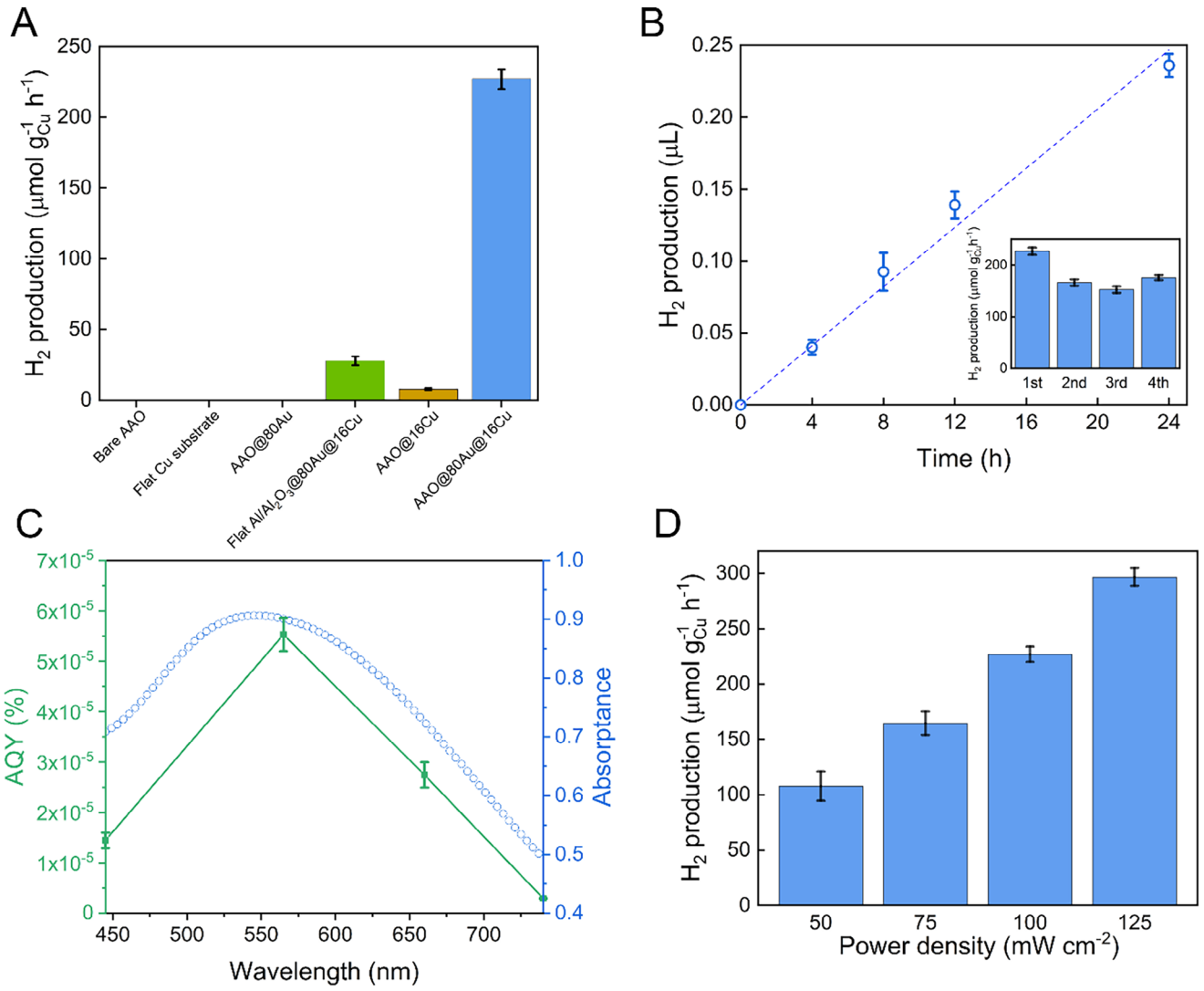

Figure 3. a) Comparison the photocatalytic H_2 evolution rate of AAO@80Au@16Cu with different materials, b) Time dependent photocatalytic H_2 evolution rate and stability test after 4 cycles (inset graph), c) Wavelength dependence of apparent quantum efficiency (AQE) plot (left axis) and UV–vis absorptance spectrum of (right axis), d) Photocatalytic H_2 evolution rate under 565 nm wavelength irradiation with different power density.

can be complex due to fabrication parameters. Therefore, the experimental sputtering times should be understood as representing a range of gold thicknesses, with the overall trend of an optimal thickness being consistent between theory and experiment. Although the trend of the absorption in the copper for different gold thicknesses is different (see Figure S13, Supporting Information), our electromagnetic simulations show (Figure S13, Supporting Information) that such thickness also corresponds to the configuration displaying maximum absorption within the Cu NPs that likely play a key role in the photocatalytic process.

2.3. Photocatalytic Ammonia Decomposition

Photocatalytic gas-phase ammonia decomposition reactions were performed in a batch reactor filled by pure NH_3 gas under simulated solar illumination (1 Sun, AM1.5G) and with samples having an active area of 2 cm^2. The reactions were carried out at near-room temperature (≈35 °C), as estimated from photo-induced temperature measurements using an IR sensor (see Figure S14a, Supporting Information). The amount of evolved hydrogen was measured by gas chromatography after 24 h of reaction. Details of the photocatalytic test conditions and setup are provided in the Supporting Information. **Figure 3** summarizes the key factors influencing the enhanced solar-light-driven photocatalytic activity of the AAO@80Au@16Cu sample. Figure 3A analyzes the contribution of each component within the system, providing insights into their roles in the overall photocatalytic process. Reference samples such as bare AAO and a flat copper substrate do not evolve any detectable amount of hydrogen. Notably, AAO@80Au remains inactive for ammonia decomposition, suggesting that the sole hot carrier generation from the Au platform is not sufficient to activate ammonia. In contrast, the AAO NCs featuring

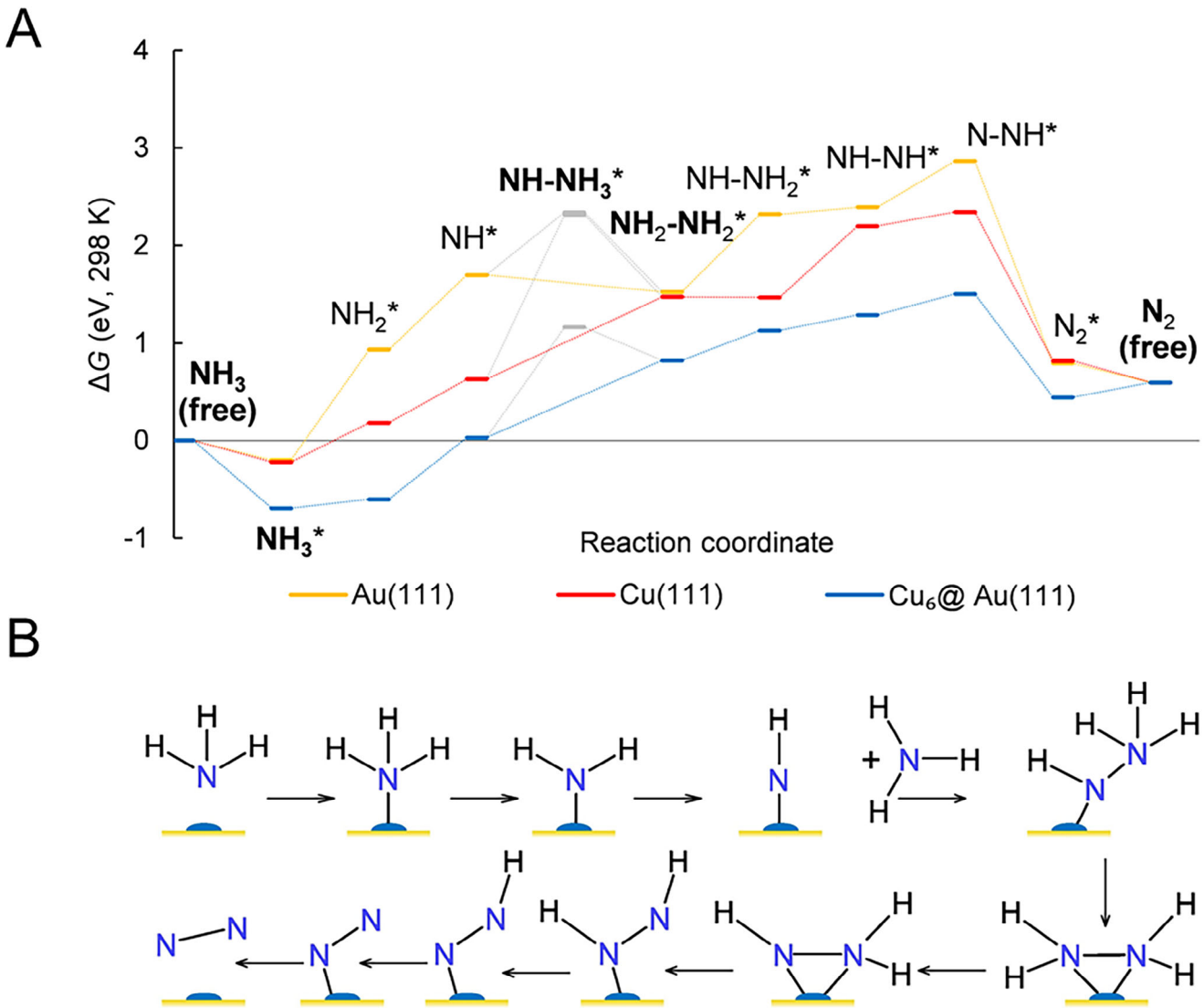

Figure 4. a) Gibbs free energy changes (ΔG) during ammonia (NH_3) decomposition on pristine Au(111) and Cu(111) surfaces, as well as on Cu_6@Au(111). b) Schematic representation of the most favorable reaction pathway on Cu_6@Au(111).

Cu nanoparticles (AAO@16Cu) produced a small amount of H_2 evolution of ≈8 μmol h^{-1} $g_{Cu}{}^{-1}$, demonstrating that the reaction active sites are on the surface of the Cu nanoparticles (reactors). Therefore, the photocatalytic rate was normalized on the amount of deposited Cu. Initial experiments were conducted to optimize the ratio of sputtered Au and Cu in the NC photocatalysts with respect to their photocatalytic activity for ammonia decomposition. The results are presented in Figure S14b,c (Supporting Information). The highest hydrogen evolution rate of 227 μmol h^{-1} $g_{Cu}{}^{-1}$ was achieved with the AAO@80Au@16Cu sample, demonstrating the synergistic interaction between Au and Cu in significantly enhancing the photocatalytic performance.

The catalytic activity of AAO@80Au@16Cu was compared with previous reports, showing a seven-times higher activity than samples tested in similar experimental conditions (Tables S2, Supporting Information), i.e. with the reaction proceeding in the gas-phase and at near-room temperature. This can be attributed to various effects. In a first instance, the morphology and composition of the catalytic interface were crucial to achieve high photocatalytic efficiency. A short Cu sputtering time (8 s) resulted in an insufficient number of active sites for photocatalysis, whereas a longer sputtering time (24 s) led to excessive Cu coverage, increasing the Cu NP size and reducing the Au-Cu interfacial sites, finally leading to decreased hydrogen evolution rates. DFT calculations suggest that the existence of a partially Cu-covered Au surface is indeed beneficial from a mechanistic perspective. The reaction pathway at the Au–Cu interface has lower activation barriers (1.16 eV for the rate-determining step of N—N bond formation) than those occurring on pristine Au(111) or Cu(111) surfaces (2.34 and 2.31 eV, respectively (**Figure** 4A). Another relevant parameter was the maximization of light absorption and field enhancement within the Cu NPs to maximize the enhancement of photocatalytic rates due to non-thermal effects. Our electromagnetic simulations show (Figure S13, Supporting Information)

that, indeed, a specific intermediate Au thickness produced the maximum absorption in the Cu NPs (Figure S13c, Supporting Information). Interestingly, we have found that such a configuration occurs when the whole nanocones maximally interact with the incident radiation (Figure S13a, Supporting Information, red line), inducing increased absorption in the Cu NPs (Figure S13c, Supporting Information) despite a relatively low absorption within the Au close to the tip (Figure S13b, Supporting Information). These findings highlight the importance of accurate antenna-reactor designs when optimizing photocatalytic processes.

To investigate further the effect of morphology on photocatalytic activity, NC-based photocatalysts were fabricated not only on sharp-tip AAO, but also on a flat Al/Al_2O_3 substrate with the same Au and Cu deposition parameters for comparison. The hydrogen evolution rate of plasmonic NCs on sharp-tip AAO was ≈7.2 times higher than that of the flat sample, suggesting a critical role of a higher surface area for the adsorption of the reactive molecules and of an ordered array of plasmonic nanostructures. Figure 3B illustrates the time-dependent evolution of H_2 production during the photocatalytic reaction using the AAO@80Au@16Cu photocatalysts. Hydrogen generation is initiated upon exposure to simulated solar light irradiation, and the amount of H_2 increases linearly over time, reaching the hydrogen evolved volume of 0.23 µL in 24 h. Furthermore, the stability and reproducibility of the system were evaluated through four repeated cycles of the ammonia decomposition reaction, confirming the catalyst's durability and consistent performance. The top-view SEM images of AAO@80Au@16Cu obtained after the reaction (Figure S14d, Supporting Information) reveal no changes in the diameter or morphology of the plasmonic NCs. This observation highlights the remarkable structural stability of the plasmonic NC array, which maintained its integrity and photoactivity even after multiple catalytic cycles. Additionally, the H_2 evolution rate during photocatalytic NH_3 decomposition was investigated under various reaction conditions, with the results presented in Figure S14e (Supporting Information). No H_2 production was observed in the dark at room temperature (25 °C) nor at a constant temperature of 50 °C provided by external heating. On the contrary, ammonia decomposition occurred only under light illumination. Such control experiments confirmed that thermal effects alone could not drive the ammonia decomposition reaction at room temperature, thus highlighting the role of plasmon-induced non-thermal effects (i.e. hot carriers and near fields). To further explore the potential role of non-thermal plasmonic effects, the H_2 evolution rate of the photocatalytic system was measured under monochromatic light conditions and expressed as the apparent quantum yield (AQY), and the results are presented in Figure 3C.

The AQY was calculated with the following equation:[36]

$$AQY = \frac{2 \times Numberof\,H_2 molecules evolved}{Numberofincidentphotons} \times 100\% \quad (2)$$

To identify the AQY depending on different wavelengths, the reaction was illuminated with different LED light sources (445, 565, 660, 740 nm). The power of the light source used for the AQY was measured via an external digital power meter (Thorlabs PM100D). The sample was illuminated for 24 h with an illuminated surface area of 2 cm^2. A low H_2 evolution rate, corresponding to a low AQY, was observed at a wavelength of 445 nm, while the maximum rate occurred at 565 nm, namely at the spectral position of the plasmonic resonance of the AAO@80Au@16Cu NC substrate.

The AQY plot well resembled the absorptance profile, indicating a strong correlation between photocatalytic activity and plasmonic resonance. The highest AQY of 5.5×10^{-5} % was observed at a wavelength of 565 nm, which is ≈4 times higher than the AQY at 740 nm. Furthermore, the dependence of the H_2 evolution rate on power density at a wavelength of 565 nm was investigated by varying the incident light power density from 50 to 125 mW cm^{-2} (Figure 3D). The linear dependence of the H_2 evolution rate on power density is consistent with a non-thermal enhancement mechanism of the catalytic reaction, while an Arrhenius-like exponential dependence should be observed in case of a purely thermally-driven mechanism.

3. Ammonia Decomposition Mechanism

To elucidate the mechanism of ammonia decomposition driven by AAO@80Au@16Cu NCs, a comprehensive surface characterization was carried out. First, X-ray photoelectron spectroscopy (XPS) experiments were performed to examine the elemental composition both before and after the reaction (Figures S16 and S17, Supporting Information). High-resolution Au 4f spectra (Figures S16a and S17a, Supporting Information) did not show any binding energy variation, indicating that Au^0 was unaffected throughout the process. The peaks corresponding to Cu 2p3/2 and Cu 2p1/2 at 932.5 and 952.3 eV, respectively, confirm the presence of the Cu^0 oxidation state after reaction (Figure S17b, Supporting Information). Those peaks were also consistent with the pure metallic Cu before reaction (Figure S16b, Supporting Information). Additionally, a small peak at 934.9 eV with a weak satellite at 944.2 eV was assigned to the Cu^{2+} form from native oxide layer on the surface.[37–38] The small shift of Cu^{2+} peak after reaction can be due to adsorbed N species remaining onto the catalyst surface and to their structural reconstruction under reaction conditions, as suggested by our DFT calculations.

Remarkably, the N 1s XPS spectra (Figure S17c, Supporting Information) revealed the emergence of two distinct peaks at 398.6 and 400.2 eV after the reaction, in stark contrast to the flat spectrum measured from the bare sharp tip AAO and pristine plasmonic NCs sample (Figures S15c and S16c, Supporting Information). Those two peaks can be attributed to the formation of NH_x (x = 1, 2) species during the dehydrogenation of NH_3, or to the dimerization process occurring during the photocatalytic reaction, leading to the formation of H_yNNH_z species (e.g. H_2NNH_2, HNNH, etc.).[39–40] Figure S16 (Supporting Information) presents the X-ray diffraction spectra of the bare sharp tip AAO substrate and the pristine AAO@80Au@16Cu sample. In addition to the most prominent peaks corresponding to metallic aluminum, a small peak associated with metallic Cu is also observed, confirming the previously discussed XPS data.

Time-of-flight secondary ion mass spectrometry (TOF-SIMS) measurements were conducted to investigate more in detail the chemical nature of such potential intermediate nitrogen compounds detected by XPS. The analysis revealed the presence of several intermediate nitrogen species, including NH_2,

NH, NNH, and HNNH, on the catalyst surface after the reaction. These findings suggest that our plasmonic nanocone array promoted an NH_3 dimerization process to form N—N bonds, and subsequent deprotonation leading to the production of H_2 and N_2 (Figure S19, Supporting Information).[41–44] In previous studies, NH_3 decomposition typically occurs at high temperatures and low ammonia partial pressures, making it challenging to directly observe the coupling of nitrogen species, including specific reaction intermediates. Consequently, the mechanistic reaction pathway has often been inferred, relying primarily on the splitting of NH_3 into N and H, which subsequently recombine to form N_2 and H_2.[9]

Spin-polarized density functional theory (SP-DFT) was employed to provide further insights into the mechanism of NH_3 decomposition, with a focus on identifying the most favorable reaction pathway from among several configurations evaluated for each reaction step. A detailed description of the DFT calculation procedures and their specific steps is provided in the Supporting Information, supported by Figures S20–S28 and Tables S3 and S4.

Changes in Gibbs free energy (ΔG at 298 K and 1 atm, Figure 4) reveal that the adsorption of NH_3 molecules on all considered surfaces is exergonic, driven by weak covalent interactions. However, the subsequent H dissociation steps on pristine Au(111) and Cu(111) surfaces are endergonic, rendering the overall reaction non-spontaneous under the considered conditions. The critical step in the decomposition of NH_3 is the formation of an N—N bond, which becomes favorable only after the formation of intermediates such as NH_2 or NH, subsequently leading to the formation of NH_2NH_2 or $NHNH_3$.[45–46] In contrast, on Cu6@Au(111), two consecutive dissociation steps result in a configuration with an adsorbed NH intermediate and a ΔG of only 0.03 eV, indicating that dissociative adsorption becomes nearly thermodynamically neutral in the presence of Cu nanoparticles.

Through DFT-base examination of various reaction pathways involving NH_3, NH_2, and/or NH intermediates, we identified the most plausible mechanism for N—N bond formation to begin with the adsorption of an NH_3 molecule onto a pre-adsorbed NH intermediate, forming an $NHNH_3$ complex. This is followed by a spontaneous hydrogen transfer, resulting in the formation of a stable hydrazine (NH_2–NH_2) molecule. Given that hydrogen transfer is typically fast, it is also possible that NH_3 adsorption leads directly to NH_2–NH_2, bypassing the $NHNH_3$ intermediate and lowering the reaction barrier.

Importantly, the N—N bond forms through the lone pair on the NH_3 nitrogen attacking the NH intermediate to form a donor–acceptor bond. This is the only viable orbital interaction pathway, as NH_3 lacks other accessible bonding orbitals. For this to occur, the NH intermediate must possess a positively charged nitrogen capable of accepting the lone pair. Density of states (DOS) analysis (Figure S29a, Supporting Information) confirms that the NH intermediate has occupied states near the Fermi energy (E_F) that become unoccupied under local potential changes in the vicinity of the N atom, facilitating electron donation from NH_3.

Charge density difference analysis (Figure S29a, Supporting Information) further supports this picture: upon single-electron removal from the system (simulating a photoexcited hot hole), the region with the greatest increase in positive charge is localized on the NH intermediate. This suggests that a plasmonic hot hole transfer may be essential for initiating the N—N bond formation. Moreover, the charge redistribution upon the N—N bond formation (Figure S29d, Supporting Information) shows a decrease in electron density between the two nitrogen atoms. Unlike standard covalent bond formation, this decrease reflects the replacement of two lone pairs—one from NH and one from NH_3—with a shared bonding electron pair, which helps explain the endergonic character of this step.

Bader charge analysis further corroborates the proposed mechanism. Upon NH_3 adsorption on NH, significant charge redistribution occurs. The NH_3 unit becomes positively charged (+0.54e), with minimal change in hydrogen atom charges (0.44 vs. 0.39 e in free NH_3), and a notable reduction in nitrogen's negative charge (–0.78 vs. –1.17e). Simultaneously, the NH group also becomes more positive (–0.76 vs –0.37e), with N and H carrying –0.80 and 0.43e, respectively. The resulting $NHNH_3$ species exhibit a net positive charge of +0.17e, indicating charge donation from nitrogen atoms to the metallic substrate. DOS analysis (Figure S29c, Supporting Information) further confirms the hybridization and N—N bond formation.

Once hydrazine forms, the reaction may reverse—releasing NH_3—or proceed via further H dissociation to form NH–NH. Under high NH_3 partial pressure, i.e. as per our experimental conditions, the forward reaction is favored. The partial pressure of gas-phase NH3 favors the latter pathway. Although dissociation of the penultimate hydrogen is thermodynamically uphill, it is plausible that the final two hydrogen atoms are released simultaneously due to their close proximity (≈2 Å) and orientation. This leads to adsorbed N_2, and the final step—N_2 desorption and catalyst regeneration—is only slightly endergonic. Notably, the reaction barrier on Cu-decorated systems is significantly lower than on pristine surfaces, confirming the catalytic advantage conferred by Cu modification.

4. Conclusion

In this study, a plasmonic NC array substrate was successfully fabricated through a facile sputtering method onto the sharp tips of an AAO template. Structural characterization using SEM, TEM, and HAADF imaging confirmed the high homogeneity and reproducibility of the plasmonic NCs on a large scale, extending up to the centimeter scale. The optical properties of the substrate were effectively controlled by adjusting the metal loading during sputtering. An optimal sputtering time corresponding to a specific Au thickness was found, effectively balancing the field enhancement in the AAO and light harnessing within the catalytic Cu NPs, as suggested by electromagnetic simulations. The photocatalytic activity of the plasmonic NCs was demonstrated through H_2 evolution from NH_3 decomposition under 1 Sun irradiation, highlighting the efficient utilization of hot carriers even at low temperatures. Finally, the combination of XPS, TOF-SIMS analysis, and DFT simulations provided valuable insights into the underlying reaction mechanisms. These findings not only enhance our understanding of light-driven NH_3 decomposition under mild conditions, but also offer a scalable alternative to the conventional thermal NH_3 decomposition mechanism, therefore opening the way to cheap and decentralized reactors driven by sunlight.

Supporting Information

Supporting Information is available from the Wiley Online Library or from the author.

Acknowledgements

The authors acknowledge the financial support of the European Union under the REFRESH – Research Excellence For Region Sustainability and High-tech Industries project number CZ.10.03.01/00/22_003/0000048 via the Operational Programme Just Transition. The study was further supported by the project TECHSCALE (CZ.02.01.01/00/22_008/0004587) via the Operational Programme Johannes Amos Comenius. Computational part of this work was supported by the Ministry of Education, Youth and Sports of the Czech Republic through the e-INFRA CZ (ID:90254). Petr Bábor acknowledges CzechNanoLab Research Infrastructure (CEITEC) supported by MEYS CR (LM2023051). Andrea Schirato acknowledges the European Union's Horizon Europe research and innovation program under the Marie Skłodowska-Curie Action PATHWAYS HORIZON-MSCA-2023-PF-GF grant agreement No. 101153856. Alberto Naldoni acknowledges the support from the Project CH4.0 under the MIUR program "Dipartimenti di Eccellenza 2023-2027" (CUP: D13C2200352001) and from the European Union-NextGeneration EU Programme, the National Recovery and Resilience Plan (NRRP), Mission 4 Component 2 Investment 1.1 PRIN 2022 PNRR, Ministero dell'Università e della Ricerca (MUR), CUP D53D23017090001, ID P2022J5NAN "Refractory plasmonic metasurfaces for solar thermal catalytic CO_2 conversion" (RESOLCAT). This material is based upon work supported by the National Science Foundation under Grant No. 2346014. Jan Navrátil acknowledges the support from Palacký University Olomouc (project IGA_PrF_2025_003). Alessandro Alabastri acknowledges support from the Robert A. Welch Foundation under grant C-2224.

Open access publishing facilitated by Univerzita Palackeho v Olomouci, as part of the Wiley - CzechELib agreement.

Conflict of Interest

The authors declare no conflict of interest.

Data Availability Statement

The data that support the findings of this study are available from the corresponding author upon reasonable request.

Keywords

anodic aluminum oxide, photocatalytic ammonia decomposition, plasmonic nanomaterial array, surface plasmon resonance

Received: February 26, 2025
Revised: July 1, 2025
Published online:

[1] N.-N. Vu, S. Kaliaguine, T.-O. Do, *Adv. Funct. Mater.* **2019**, *29*, 1901825.
[2] J. K. Stolarczyk, S. Bhattacharyya, L. Polavarapu, J. Feldmann, *ACS Catal.* **2018**, *8*, 3602.
[3] G. Zhao, K. Rui, S. X. Dou, W. Sun, *Adv. Funct. Mater.* **2018**, *28*, 1803291.
[4] S. Nishioka, F. E. Osterloh, X. Wang, T. E. Mallouk, K. Maeda, *Nature Reviews Methods Primers* **2023**, *3*, 42.
[5] Y. Liu, Z. Wei, X. Su, X. Shi, L. Liu, T. Wang, X. Xu, M. Zhao, Y. Zhai, H. B. Yang, B. Liu, *Adv. Funct. Mater.* **2024**, *n/a*, 2403547.
[6] M. Dong, J. Zhou, J. Zhong, H.-T. Li, C.-Y. Sun, Y.-D. Han, J.-N. Kou, Z.-H. Kang, X.-L. Wang, Z.-M. Su, *Adv. Funct. Mater.* **2022**, *32*, 2110136.
[7] R. Hren, A. Vujanović, Y. Van Fan, J. J. Klemeš, D. Krajnc, L. Čuček, *Renewable Sustainable Energy Rev.* **2023**, *173*, 113113.
[8] H. Wang, J. Li, X. Wei, Y. Zheng, S. Yang, Y. Lu, Z. Ding, Q. Luo, Q. Li, F. Pan, *Adv. Funct. Mater.* **2024**, *34*, 2406639.
[9] I. Lucentini, X. Garcia, X. Vendrell, J. Llorca, *Ind. Eng. Chem. Res.* **2021**, *60*, 18560.
[10] F. Chang, W. Gao, J. Guo, P. Chen, *Adv. Mater.* **2021**, *33*, 2005721.
[11] T. He, P. Pachfule, H. Wu, Q. Xu, P. Chen, *Nat. Rev. Mater.* **2016**, *1*, 16059.
[12] W. Chen, X. Yang, Z. Chen, Z. Ou, J. Hu, Y. Xu, Y. Li, X. Ren, S. Ye, J. Qiu, J. Liu, Q. Zhang, *Adv. Funct. Mater.* **2023**, *33*, 2300512.
[13] L. He, X. Zeng, H. Chen, L. Zhao, Z. Huang, D. Wang, X. He, W. Fang, X. Du, W. Li, *Adv. Funct. Mater.* **2024**, *34*, 2313058.
[14] A. M. Karim, V. Prasad, G. Mpourmpakis, W. W. Lonergan, A. I. Frenkel, J. G. Chen, D. G. Vlachos, *J. Am. Chem. Soc.* **2009**, *131*, 12230.
[15] P. Xie, Y. Yao, Z. Huang, Z. Liu, J. Zhang, T. Li, G. Wang, R. Shahbazian-Yassar, L. Hu, C. Wang, *Nat. Commun.* **2019**, *10*, 4011.
[16] K. Nagaoka, T. Eboshi, Y. Takeishi, R. Tasaki, K. Honda, K. Imamura, K. Sato, *Sci. Adv.* *3*, 1602747.
[17] C. Zhan, X.-J. Chen, J. Yi, J.-F. Li, D.-Y. Wu, Z.-Q. Tian, *Nat. Rev. Chem.* **2018**, *2*, 216.
[18] X.-C. Ma, Y. Dai, L. Yu, B.-B. Huang, *Light: Sci. Appl.* **2016**, *5*, 16017.
[19] U. Aslam, V. G. Rao, S. Chavez, S. Linic, *Nat. Catal.* **2018**, *1*, 656.
[20] P. Christopher, H. Xin, S. Linic, *Nat. Chem.* **2011**, *3*, 467.
[21] L. Zhou, J. M. P. Martirez, J. Finzel, C. Zhang, D. F. Swearer, S. Tian, H. Robatjazi, M. Lou, L. Dong, L. Henderson, P. Christopher, E. A. Carter, P. Nordlander, N. J. Halas, *Nat. Energy* **2020**, *5*, 61.
[22] L. Zhou, D. F. Swearer, C. Zhang, H. Robatjazi, H. Zhao, L. Henderson, L. Dong, P. Christopher, E. A. Carter, P. Nordlander, N. J. Halas, *Science* **2018**, *362*, 69.
[23] Y. Yuan, L. Zhou, H. Robatjazi, J. L. Bao, J. Zhou, A. Bayles, L. Yuan, M. Lou, M. Lou, S. Khatiwada, E. A. Carter, P. Nordlander, N. J. Halas, *Science* **2022**, *378*, 889.
[24] Y. Dubi, I. W. Un, Y. Sivan, *Chem. Sci.* **2020**, *11*, 5017.
[25] L. Mascaretti, A. Schirato, T. Montini, A. Alabastri, A. Naldoni, P. Fornasiero, *Joule* **2022**, *6*, 1727.
[26] A. B. Taylor, A. M. Siddiquee, J. W. M. Chon, *ACS Nano* **2014**, *8*, 12071.
[27] H. Masuda, K. Fukuda, *Science* **1995**, *268*, 1466.
[28] W. Lee, S.-J. Park, *Chem. Rev.* **2014**, *114*, 7487.
[29] M. Kaur, S. Ishii, S. L. Shinde, T. Nagao, *Adv. Sustainable Syst.* **2019**, *3*, 1800112.
[30] L. Zhou, Y. Tan, D. Ji, B. Zhu, P. Zhang, J. Xu, Q. Gan, Z. Yu, J. Zhu, *Sci. Adv.* **2016**, *2*, 1501227.
[31] K. Bae, G. Kang, S. K. Cho, W. Park, K. Kim, W. J. Padilla, *Nat. Commun.* **2015**, *6*, 10103.
[32] H. Tang, G. Shao, B. J. Hinds, *Adv. Funct. Mater.* **2021**, *31*, 2100342.
[33] H. Jia, Z. Li, B. Wang, G. Xing, Y. L. Wong, H. Ren, M. Li, K.-Y. Wong, D. Lei, L.-W. Wong, J. Zhao, W. Zhang, S. Sang, A. Jian, X. Zhang, *ACS Photonics* **2022**, *9*, 652.
[34] M. Go, I. Hong, D. Lee, S. Kim, J. Jang, K.-W. Kim, S. Shim, K. Yong, J. Rho, J. K. Kim, *NPG Asia Mater.* **2024**, *16*, 4.
[35] J. Zhou, Y. Gu, P. Liu, P. Wang, L. Miao, J. Liu, A. Wei, X. Mu, J. Li, J. Zhu, *Adv. Funct. Mater.* **2019**, *29*, 1903255.
[36] Y.-G. Yu, G. Chen, L.-X. Hao, Y.-S. Zhou, Y. Wang, J. Pei, J.-X. Sun, Z.-H. Han, *Chem. Commun.* **2013**, *49*, 10142.
[37] B. Yu, J. Diniz, K. Lofgren, Q. Liu, R. Mercado, F. Nichols, S. R. J. Oliver, S. Chen, *ACS Sustainable Chem. Eng.* **2022**, *10*, 15501.
[38] K. Chung, J. Bang, A. Thacharon, H. Y. Song, S. H. Kang, W.-S. Jang, N. Dhull, D. Thapa, C. M. Ajmal, B. Song, S.-G. Lee, Z. Wang, A.

Jetybayeva, S. Hong, K. H. Lee, E. J. Cho, S. Baik, S. H. Oh, Y.-M. Kim, Y. H. Lee, S.-G. Kim, S. W. Kim, *Nat. Nanotechnol.* **2022**, *17*, 285.
[39] L. S. Kibis, D. A. Svintsitskiy, A. I. Stadnichenko, E. M. Slavinskaya, A. V. Romanenko, E. A. Fedorova, O. A. Stonkus, V. A. Svetlichnyi, E. D. Fakhrutdinova, M. Vorokhta, B. Šmíd, D. E. Doronkin, V. Marchuk, J.-D. Grunwaldt, A. I. Boronin, *Catal. Sci. Technol.* **2021**, *11*, 250.
[40] S. Zhang, F. Xing, L. Chen, X. Wang, X. He, *Chem. Mater.* **2022**, *34*, 9031.
[41] A. Estejab, G. G. Botte, *Mol. Catal.* **2018**, *445*, 279.
[42] J. A. Herron, P. Ferrin, M. Mavrikakis, *J. Phys. Chem. C* **2015**, *119*, 14692.
[43] K. Yang, J. Liu, B. Yang, *J. Catal.* **2022**, *405*, 626.
[44] C. Zhan, X.-J. Chen, Y.-F. Huang, D.-Y. Wu, Z.-Q. Tian, *Acc. Chem. Res.* **2019**, *52*, 2784.
[45] J. L. Bao, E. A. Carter, *ACS Nano* **2019**, *13*, 9944.
[46] L. Yuan, J. Zhou, M. Zhang, X. Wen, J. M. P. Martirez, H. Robatjazi, L. Zhou, E. A. Carter, P. Nordlander, N. J. Halas, *ACS Nano* **2022**, *16*, 17365.